Journal of Applied Fluid Mechanics, Vol. 16, No. 11, pp. 2189-2205, 2023.
Available online at www.jafmonline.net, ISSN 1735-3572, EISSN 1735-3645.
https://doi.org/10.47176/jafm.16.11.1936

Effect of Blade Trimming Length on the Performance of Marine Centrifugal Pump

L. J. Zhai[1], H. X. Chen [1†], Q. Gu[1] and Z. Ma[2]

[1] *Shanghai Key Laboratory of Mechanics in Energy Engineering, Shanghai Institute of Applied Mathematics and Mechanics, School of Mechanics and Engineering Science, Shanghai University, Shanghai, Shanghai 200072, China*
[2] *Chinese Ship Scientific Research Center, Shanghai, Shanghai 200011, China*

†*Corresponding Author Email: chenhx@shu.edu.cn*

ABSTRACT

To study the hydrodynamic characteristics of blade trimming length in centrifugal pumps, Delayed Detached Eddy Simulation (DDES) with nonlinear eddy viscosity was utilized to conduct unsteady calculations on the centrifugal pump. A comprehensive examination of the fluid dynamic properties of the centrifugal pump, including external features, flow conditions, and pressure fluctuations, was carried out. By applying the theory of entropy production, the areas of high energy loss within the centrifugal pump were identified, and the correlations between local entropy production, energy loss, and unsteady flow in different areas with varying blade trimming lengths were analyzed. The results indicate that with the increase in blade trimming length, under rated flow conditions, the head decreases by 1.8%, 3.2%, and 5.7% for different blade trimming lengths, respectively, compared to normal impellers. Similarly, the efficiency decreases by 0.5%, 0.8%, and 1.0% for different blade trimming lengths, respectively. Similar trends were observed under other working conditions as well. As the degree of blade trimming increases, the irreversible losses after the failure of the centrifugal pump also increase significantly, indicating that the flow inside the centrifugal pump becomes disorder. Blade trimming leads to a disorderly fluid flow inside the centrifugal pump, causing an increase in the radial force during operation, which in turn leads to an increase in vibration amplitude and affects its operational stability. Blade trimming failure has a significant impact on the frequency and amplitude of pressure pulsation, resulting in abnormal pressure pulsation and abnormal vibration of the centrifugal pump. Therefore, early warning and diagnosis of blade trimming can be achieved through pressure pulsation monitoring.

Article History

Received April 19, 2023
Revised June 29, 2023
Accepted July 16, 2023
Available online September 3, 2023

Keywords:

Marine centrifugal pump trimming impeller
Numerical simulation
Entropy production
Energy loss

1. INTRODUCTION

Centrifugal pumps, serving as versatile devices that convert the energy from a prime mover into fluid energy, find wide-ranging applications across various fields (Chen et al., 2023; Li et al., 2023; Wang et al., 2023). Marine centrifugal pumps have more demanding requirements in terms of design, manufacturing, installation, and operation compared to ordinary centrifugal pumps. This is attributed to the constraints posed by ship cabin space, operating environment, and specific performance requirements. These requirements include small volume and weight, low vibration and noise levels, adaptability to varying ship operating conditions from berthing to full speed, corrosion resistance, anti-cavitation capability, impact resistance, and high reliability (Chen, 2020). In marine mechanical facilities, pumps account for approximately 20% to 30% of the total equipment, with centrifugal pumps comprising about 70% of them (Zhang, 2017). Centrifugal pumps used on board frequently operate under harsh conditions, resulting in a series of operational failures. According to statistical analysis (Aenis et al., 2002; Li et al., 2023), blade failures in centrifugal pumps account for over 65% of impeller mechanical failures, leading to significant accidents and losses. The causes of blade failures in centrifugal pumps are primarily attributed to three factors. Firstly, the high-frequency and prolonged operation of centrifugal pumps subjects them to intermittent vibrations. Over time, this can lead to the loosening or detachment of impeller fastening screws, causing the impeller to deviate from its intended rotational path. As a consequence, mechanical friction occurs, leading to blade fractures within the

NOMENCLATURE

K	Turbulent kinetic energy	LES	Large Eddy Simulation
μ_t	Eddy viscosities	DES	Detached Eddy Simulation
ρ	Density	DDES	Delayed Detached Eddy Simulation
$\bar{u}$	The mean velocity	NLEVM	Non-Linear Eddy Viscosity Model
P	Static pressure	DDES_NL	The DDES model based on NLEVM
RANS	Reynolds-averaged Navier-Stokes	SST	Shear-Stress Transport

pump body (Feng, 2021). Secondly, the internal forces within the pump body during operation are highly complex. The pressure difference formed between the front and the rear sections of the blade, resulting from various forces, exposes the blade to alternating stresses. This cyclic loading can lead to fatigue and increase the susceptibility of the blade to failure (Hu, 2009). Thirdly, centrifugal pumps often operate in outdoor environments for extended periods. Consequently, internal mechanical structures may experience rusting or damage to the filtration devices. This can introduce solid impurities into the medium being pumped, further exacerbating the likelihood of blade failure. When these failures occur, they can cause unstable fluid flow and abnormal vibrations, further damaging the centrifugal pump. This can potentially impact the safety and stability of vessel operations (Yang, 2019). Therefore, in recent years, studying the characteristics of centrifugal pumps under fault conditions has become a popular topic.

Recently, researchers from around the world have conducted extensive investigations into the characteristics of centrifugal pumps under faulty conditions using various methods, including theoretical analysis, experiments, and numerical simulations. Muralidharan et al. (2011) employed support vector machines to diagnose faults in single-stage centrifugal pumps, including bearing faults, impeller defects, bearing and impeller defects, and cavitation. Li et al. (2018) utilized multi-scale multi-symbol dynamic entropy (MvMSDE) to extract failure characteristics of centrifugal pumps, such as inner race crack fault (CFIR), outer race crack fault (CFOR), cover plate defect of impeller (CPDI), and blade defect of impeller (BDI), for diagnostic purposes. Zhu (2016) analyzed the causes of low operating efficiency and severe energy loss in multi-stage centrifugal pumps and proposed a multi-parameter fusion fault diagnosis method for common faults affecting operating efficiency, namely blade fracture, impeller blockage, cavitation, and wear of the throat bush. Araste et al. (2020) introduced a multi-fault classification method based on support vector machines (SVM) for diagnosing faults in centrifugal pumps, including blade end faults, cracks, leaks, and cavitation. Jamimoghaddam et al. (2020) presented a data-driven anomaly detection method for diagnosing faults in centrifugal pumps, including blade end faults, impeller crack faults, and cavitation. This method employed the Entropy Signal Analysis (ESA) technique and the Self-Organizing Map (SOM) algorithm for fault detection. Lan (2020) used the RNG K-ε turbulence model to numerically model blade wear faults in centrifugal pumps. The study revealed that blade wear faults primarily resulted in decreased performance parameters of the pump, uneven pressure and velocity distribution in adjacent flow channels of the trimming blades, and reduced pressure and velocity in the volute area. Zabihihesari et al. (2020) investigated the impact of blade tip faults on fluid flow patterns through numerical simulations and determined the optimal position of vibration sensors for detecting impeller faults in centrifugal pumps. The method employed finite element analysis and simulation techniques, which were validated through experiments. Cao et al. (2020) proposed a fault diagnosis method combining principal component analysis (PCA) and Gaussian mixture model (GMM), integrating signal processing and knowledge for diagnosing centrifugal pump crack faults. Yang (2019) employed the RNG K-ε turbulence model to numerically simulate 1/2 blade wear faults in centrifugal pumps and observed significant fluctuations in pressure pulsation and a smaller peak value compared to normal operating conditions. This study provided a theoretical foundation for optimizing design and fault diagnosis of centrifugal pumps. Wu et al. (2021) studied the operating characteristics of centrifugal pumps with fractured impellers through tests and numerical simulations. The study investigated energy characteristics, vibration, internal flow, pressure fluctuations, and radial forces, among other aspects. Tan et al. (2020) examined the performance and internal flow characteristics of single-stage single-suction centrifugal pumps with various issues, such as blade breakage and throat bush wear, utilizing testing and numerical simulations.

With the continuous advancement of entropy production theory and the refinement of entropy production models, research based on this theory is gaining increasing recognition and widespread application in numerical studies of fluid machinery. Entropy production, as a valuable tool for quantifying irreversibility, can be utilized to analyze energy losses in flow and heat transfer designs, as well as to diagnose the location and spatial distribution of irreversible losses occurring during the flow process. Consequently, optimization designs based on entropy production theory and the diagnosis of adverse flow are increasingly employed, offering a fresh perspective for enhancing equipment performance and optimization. Brizuela (1993) employed numerical methods to investigate the distribution of entropy production in the impeller of a centrifugal pump and identified that entropy production primarily occurred near the front cover plate wall and the blade tip gap. Wallace & Davies (1997) proposed a method for calculating the entropy production rate in the boundary layer of an incompressible laminar turbine blade. Zhang et al. (2011) demonstrated through numerical results on energy conversion characteristics,

that energy losses in the impeller arise from wall friction, with the middle and outlet of the impeller being the main regions where work is performed, while the efficiency of energy conversion at the inlet of the impeller is the lowest. Behzadmehr & Mercadier (2009) analyzed the entropy production of a backward curved blade centrifugal fan and emphasized the significance of considering the dissipation term, indicating that the entropy production method can be employed to diagnose the location of energy losses and guide the optimization and enhancement of fan efficiency. Wang et al. (2011) utilized numerical simulations and combined entropy production theory with optimization algorithms to optimize the design of a centrifugal fan. The optimized fan exhibited significantly reduced entropy production in the impeller and volute, resulting in reduced flow losses. Zhou et al. (2022) introduced entropy production theory in the numerical simulation of hydraulic turbines, emphasizing its ability to analyze flow losses more intuitively and provide detailed insights into flow losses inside the hydraulic turbine. Gong et al. (2013) also utilized entropy production theory to analyze energy losses in a hydraulic turbine and identified that head impact losses in the impeller and flow separation at the tail are the primary reasons for energy losses inside the rotor. They highlighted the usefulness of entropy production theory for quantitative and localized analysis of energy dissipation within the hydraulic turbine. Ohiemi et al. (2023) investigate the assessment of energy losses in a low-pressure axial turbine with varying numbers of blades using the entropy generation method. The study reveals a trade-off relationship between blade numbers and system efficiency. Wang et al. (2023) present a numerical investigation of the energy characteristics of a centrifugal pump for cavitation flow using the entropy production theory. The study aims to explore the energy losses and cavitation phenomena in a vortex flow centrifugal pump under different operating conditions. Wang et al. (2023) provide a case study of a micro horizontal axis river ducted turbine, assessing energy loss using the entropy production theory. The research aims to explore the performance characteristics and energy loss of micro turbines in a river environment.

Currently, the majority of research on centrifugal pumps has focused on fault detection and operational characteristics, while the investigation of blade trimming length in ship-use centrifugal pumps has received limited attention. This paper aims to address this gap by conducting a comprehensive study on the influence of blade trimming length on the performance of centrifugal pumps. In this study, the entropy production theory is employed to analyze the energy loss in the centrifugal pump and explore the correlation between its internal flow field and the blade trimming length. By utilizing this theory, the researchers aim to gain insights into the energy dissipation and flow behavior associated with different levels of blade damage. The findings of this study contribute to the field of fault diagnosis in centrifugal pumps, providing valuable references for future research in this area.

2. NUMERICAL METHODS

It is widely recognized that Reynolds-averaged Navier-Stokes (RANS) models are not effective in modeling separated flows, while large eddy simulation (LES) models can be computationally expensive when dealing with high Reynolds number wall-bounded flows. To address these issues, researchers have extensively studied hybrid methods that combine the benefits of both RANS and LES models. One such method is detached eddy simulation (DES), which was originally proposed by Spalart et al. (1997). DES utilizes unsteady RANS models for the boundary layer and employs LES treatment for separated regions to avoid the high cost of solving wall turbulence. To address the separation problem that occurs due to meshing in the original DES method, Seo & Lee (2019) developed a delayed detached eddy simulation (DDES).

2.1 The DDES with a Non-Linear Eddy Viscosity Model (DDES_NL)

By including the dissipation term of the k equation (Wang, 2019), the Shear Stress Transport k-ω model has been modified, and the governing equations can be expressed as follows:

$$\frac{\partial(\rho k)}{\partial t}+\frac{\partial(\rho u_j k)}{\partial x_j}=\tilde{P}_k-\beta^*\rho k\omega F_{(Delayed)DES} +\frac{\partial}{\partial x_j}[(\mu+\sigma_k\mu_t)\frac{\partial k}{\partial x_j}] \tag{1}$$

$$\frac{\partial(\rho\omega)}{\partial t}+\frac{\partial(\rho u_j\omega)}{\partial x_j}=\alpha\rho S^2-\beta\rho\omega^2+ \frac{\partial}{\partial x_j}[(\mu+\sigma_\omega\mu_t)\frac{\partial\omega}{\partial x_j}]+2(1-F_1)\rho\sigma_{\omega2}\frac{1}{\omega}\frac{\partial k}{\partial x_j}\frac{\partial\omega}{\partial x_j} \tag{2}$$

$F_{(Delayed)DES}$ is a delay function defined as follows:

$$F_{(Delayed)DES}=\max\left(\frac{l_{SST}}{l_{LES}}\cdot(1-F_1),1\right) \tag{3}$$

The turbulence length scale for the SST k-ω model is given below:

$$l_{SST}=\frac{\sqrt{k}}{\beta^*\omega} \tag{4}$$

The turbulence length scale of LES is:

$$l_{LES}=C_{DES}\Delta \tag{5}$$

The model constants are calibrated $C_{DES}=0.61$ in the SST k-ω model. The blending function F_1 is defined as follows:

$$F_1=\tanh\left\{\left\{\min[\max(\frac{\sqrt{k}}{\beta^*\omega y},\frac{500\upsilon}{y^2\omega}),\frac{4\rho\sigma_{\omega2}k}{CD_{k\omega}y^2}]\right\}^4\right\} \tag{6}$$

Where $CD_{k\omega}=\max(2\rho\sigma_{\omega 2}\frac{1}{\omega}\frac{\partial k}{\partial x_i}\frac{\partial \omega}{\partial x_i},10^{-10})$ and y is the distance to the nearest wall. Then, the eddy viscosity μ_t is calculated by

$$\mu_t=\frac{\rho a_1 k}{\max(a_1\omega,SF_2)} \tag{7}$$

Where $S^2=2S_{ij}S_{ij}$ for $S_{ij}=\frac{1}{2}(\frac{\partial \overline{u}_i}{\partial x_j}+\frac{\partial \overline{u}_j}{\partial x_i})$ and F_2 is the second blending function is defined as follows

$$F_2=\tanh\left\{\left\{\max(\frac{2\sqrt{k}}{\beta^*\omega y},\frac{500\upsilon}{y^2\omega})\right\}^2\right\} \tag{8}$$

The constants are blended by the relation $f=f_1F_1+f_2(1-F_1)$ where f can be constants σ_k, σ_ω, β, and γ. The constants used in the model are as follows: $\beta_1=0.075$, $\beta_2=0.0828$, $\sigma_{k1}=0.85$, $\sigma_{k2}=1.0$, $\sigma_{\omega 1}=0.5$, $\sigma_{\omega 2}=0.856$, $\beta^*=0.09$, $\gamma_1=5/9$, $\gamma_2=0.44$, and $\alpha_1=0.31$.

Due to its linear eddy viscosity-based nature, the prediction accuracy of the DDES model is limited when it comes to flows with significant pressure gradients. To overcome this limitation, Zhai et al. (2022) incorporated a non-linear eddy viscosity model into the DDES model originally proposed by Wei et al. (2016) The non-linear eddy viscosity model was developed based on experiments (Champagne et al., 1970; Tavoularis & Corrsin, 1981) and the DNS (Rogers & Moin 1987; Lee et al., 1990).The expression of the eddy viscosity coefficient C_μ which is a piecewise function is given as follows:

$$C_\mu=0.00099+\begin{cases}\dfrac{0.09401}{\left(1+\left(\frac{\eta}{5.2}\right)^{6.1}\right)}, \eta\le 4.4\\ 0.2\times\exp(-\frac{\eta}{3.05})+0.03\times\exp(-\frac{\eta}{15.5}), \eta\ge 4.4\end{cases} \tag{9}$$

$$\eta=\sqrt{\frac{1}{2}(\tilde{S}^2+\tilde{\Omega}^2)} \tag{10}$$

$$\tilde{S}=\sqrt{2\tilde{S}_{ij}\tilde{S}_{ij}},\quad \tilde{S}_{ij}=\frac{k}{\varepsilon}S_{ij} \tag{11}$$

$$\tilde{\Omega}=\sqrt{2\tilde{\Omega}_{ij}\tilde{\Omega}_{ij}},\quad \tilde{\Omega}_{ij}=\frac{k}{\varepsilon}\Omega_{ij} \tag{12}$$

The non-linear eddy viscosity model has proven to be effective in capturing unsteady turbulent structures and making accurate predictions, as demonstrated in studies on non-stationary flows around a triangular cylinder, wind-turbine airfoil, and two-dimensional and three-dimensional centrifugal pump (Wei et al., 2015; Zhang et al., 2019a, b; Zhang et al., 2021; 2022a, b; Liu et al., 2022). Zhai et al. (2022) have also demonstrated the effectiveness and versatility of DDES with a non-linear eddy viscosity model. In this study, the simulation of the unsteady flow structures of a centrifugal pump is conducted using the Detached Eddy Simulation (DES) method with a non-linear eddy viscosity model. The implementation of the DDES method with a non-linear eddy viscosity model is achieved through the utilization of CEL (CFX Expression Language) codes.

3. ENTROPY PRODUCTION THEORY

The entropy production theory is a branch of the second law of thermodynamics that considers entropy as a state variable parameter in fluid flow. According to the second law of thermodynamics, viscosity and turbulent behavior in water flow lead to an increase in entropy due to irreversible factors, resulting in a dissipation effect during the flow process. In the case of a centrifugal pump operating at normal temperature and pressure, where the specific heat capacity of water is large, the temperature change is assumed to be constant without considering the effect of heat transfer. The Reynolds time-averaged entropy production can be separated into two components: the first component is the viscous dissipation entropy production caused by fluid viscosity, and the second component is the turbulent dissipation entropy production caused by turbulent fluctuations. These components can be calculated using the following formulas (Kock & Herwig 2004; 2005):

Viscous dissipation entropy production rate caused by fluid viscosity (W m^{-3} K^{-1}):

$$\dot{S}_{\bar{D}}'''=\frac{\mu}{T}\left[\left(\frac{\partial \overline{u}}{\partial y}+\frac{\partial \overline{v}}{\partial x}\right)^2+\left(\frac{\partial \overline{u}}{\partial z}+\frac{\partial \overline{w}}{\partial x}\right)^2+\left(\frac{\partial \overline{v}}{\partial z}+\frac{\partial \overline{w}}{\partial y}\right)^2\right]+\frac{2\mu}{T}\left[\left(\frac{\partial \overline{u}}{\partial x}\right)^2+\left(\frac{\partial \overline{v}}{\partial y}\right)^2+\left(\frac{\partial \overline{w}}{\partial z}\right)^2\right] \tag{13}$$

Turbulent dissipation entropy production rate caused by turbulent fluctuation (W m^{-3} K^{-1}):

$$\dot{S}_{D'}'''=\frac{\mu}{T}\left[\left(\frac{\partial u'}{\partial y}+\frac{\partial v'}{\partial x}\right)^2+\left(\frac{\partial u'}{\partial z}+\frac{\partial w'}{\partial x}\right)^2+\left(\frac{\partial v'}{\partial z}+\frac{\partial w'}{\partial y}\right)^2\right]+\frac{2\mu}{T}\left[\left(\frac{\partial u'}{\partial x}\right)^2+\left(\frac{\partial v'}{\partial y}\right)^2+\left(\frac{\partial w'}{\partial z}\right)^2\right] \tag{14}$$

Where: $\bar{u}$、$\bar{v}$、$\bar{w}$ are the components of mean velocity in the x, y, and z directions respectively, in units of m/s; u'、v'、w' are the components of fluctuating velocity in the x, y, and z directions respectively, in units of m/s; T is the temperature, in units of K, and is assumed to be at room temperature of 283 K for calculation purposes; μ is the dynamic viscosity of the fluid, in units of Pa s.

The viscous dissipation entropy production rate can be directly calculated in post-processing of computational fluid dynamics (CFD), but the turbulent velocity field cannot be directly solved. However, there is an internal connection between turbulent dissipation entropy production and turbulent models. Hence, in the k-ω turbulence model, the rate of entropy production caused by turbulent fluctuations can be expressed as:

$$\dot{S}_{D'}'''=\beta\frac{\rho\omega k}{T} \tag{15}$$

Where β = 0.09; ω is the turbulent kinetic energy dissipation rate, and k is the turbulent intensity (Li et al. 2021). Integrating the above two entropy production rates over the entire computational domain separately, the viscous dissipation entropy production S_{DV} (W/K) and the turbulent dissipation entropy production S_{DT} (W/K) can be obtained:

$$S_{DV} = \int_V \dot{S}_{\bar{D}}''' dV \tag{16}$$

$$S_{DT} = \int_V \dot{S}_{D'}''' dV \tag{17}$$

The entropy production and transport equation, as an alternative form of the energy equation, can be utilized for evaluating energy consumption. In comparison to traditional methods of flow field analysis, the entropy production theory enables quantitative and localized analysis of energy consumption. By accurately calculating energy consumption, it can efficiently identify positions where high energy consumption occurs. Furthermore, this method can visually present the distribution of energy consumption through field distribution, providing a more intuitive representation. Consequently, the entropy production method accomplishes functions that traditional analysis methods cannot achieve, thus holding significant research value. The entropy production theory has been introduced and applied to the fault diagnosis of centrifugal pumps used in ships.

4. TEST RIG AND RESEARCH MODEL

This section provides a detailed description of the model used in the study. The modeling of the centrifugal pump components, such as the inlet pipe, front shroud, impeller, volute, and back shroud, was carried out using the 3D modeling software Creo Parametric 3.0. The resulting model is illustrated in Fig. 1, which showcases the complete assembly of the centrifugal pump with all its relevant components. The main geometric parameters of vertical single-stage marine centrifugal pump are shown in Table 1.

Table 1 Basic parameters

Parameters	Value
Design flow rate Q_0(m^3 /h)	100
Pump design head H(m)	32
Rotating speed n(r/min)	1470
Specific speed n_s	66.7
Blade numbers Z	7
Inlet diameter of impeller D_j(mm)	94
Outlet diameter of impeller D_2(mm)	314
Volute inlet diameter D_3(mm)	324
Blade inlet width b_1 (mm)	34
Blade outlet width b_2(mm)	18
Wrap angle ϕ(°)	166.2

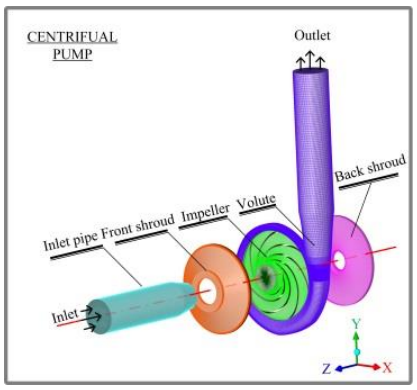

Fig. 1 Computational domain model

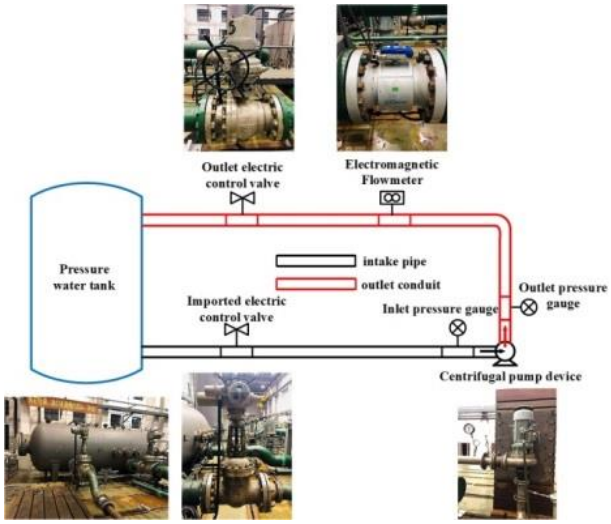

Fig. 2 Schematic diagram of centrifugal pump experimental system

The experiment was conducted at the experimental base of the 704th Research Institute of China Shipbuilding Industry Corporation. The experimental setup primarily consists of the following equipment: variable frequency motor, variable frequency starter cabinet, centrifugal pump, pressure water tank, inlet and outlet electric control valves, electromagnetic flowmeter, inlet and outlet pressure measurement tubes, and pipeline accessories, as shown in Fig 2.

The pressure sensor utilized in the experiment is the CY200 miniature pressure sensor provided by Chengdu Taiste Electronic Information Co., Ltd. It features a measurement range of 0-0.4 MPa, an accuracy of 0.25% FS (Full Scale), and a frequency response exceeding 30 kHz. The experimental pressure pulsation measurement points are labeled as Vol_3 to Vol_9, totaling 7 points. The numerical pressure pulsation measurement points are denoted as Vol_1 to Vol_12, totaling 12 points, as depicted in Fig 3.

Figure 4 shows the model and computational meshes for various degrees of damage to the normal and trimmed impellers. The original impeller outlet diameter of the experimental pump was 314 mm. However, for different degrees of damage, the trim radius was defined as follows: R_b for 150 mm, 140 mm, and 130 mm, respectively. For ease of reference, the abbreviations BB_1, BB_2, and BB_3 are used to represent impellers with a single blade trim radius of 150 mm, 140 mm, and 130

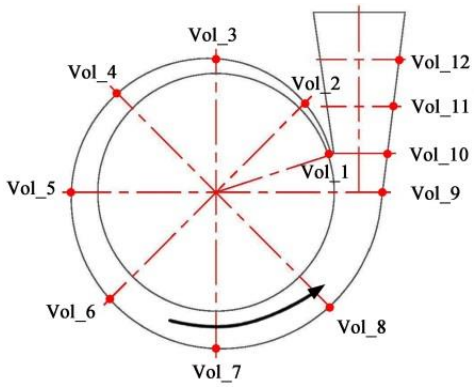

Fig. 3 Pressure fluctuation measuring points

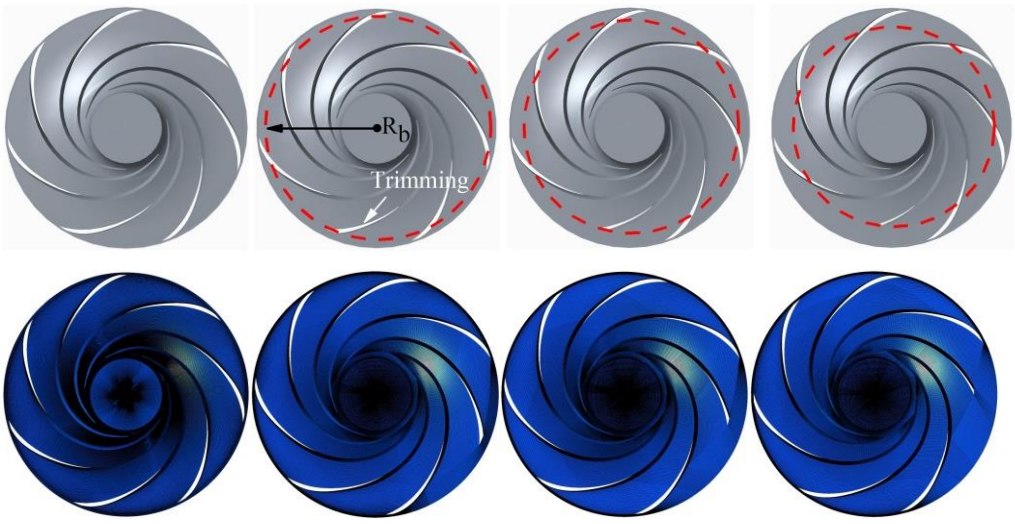

(a) NB (b) BB_1 (c) BB_2 (d) BB_3

Fig. 4 Normal impeller and trimming impeller with varying degrees

Table 2 Grids independence analysis

	Volute	Inlet pipe	Front shroud	Back shroud	Impeller	Total grid	Head(m)
Grid 1	1.32×10^6	0.70×10^6	0.33×10^6	0.12×10^6	0.41×10^6	2.88×10^6	29.7376
Grid 2	1.32×10^6	0.70×10^6	0.33×10^6	0.12×10^6	1.32×10^6	3.79×10^6	30.6825
Grid 3	1.32×10^6	0.70×10^6	0.40×10^6	0.12×10^6	2.35×10^6	4.89×10^6	31.2543
Grid 4	1.32×10^6	0.70×10^6	0.40×10^6	0.25×10^6	2.35×10^6	5.02×10^6	32.2928
Grid 5	1.32×10^6	0.70×10^6	0.40×10^6	0.25×10^6	3.42×10^6	6.09×10^6	32.1406

mm, respectively. Additionally, the abbreviation NB is used to represent the normal impeller pump model.

The ANSYS ICEM 15.0 software was utilized to generate topology and hexahedral meshes for the inlet pipe, front shroud, impeller, volute, and back shroud in the computational domain, as shown in Fig 1. Hexahedral meshing was chosen due to its advantages in preserving the orthogonality of the boundary layer, accurately fitting the body geometry, and controlling numerical dissipation. The mesh independence analysis results are summarized in Table 2, which confirms independence for the five sets of meshes. With an increase in the number of meshes, the variation in the head is found to be less than 0.5%. For subsequent calculations, a computational model consisting of 5 million grids (referred to as Grid 4) is utilized.

5. RESULTS AND ANALYSIS

5.1. External Characteristics

All numerical calculations in this study were conducted using ANSYS CFX 15.0, the CFD software. To facilitate data transfer between the moving and static parts of the centrifugal pump, the frozen rotor method was employed for steady-state calculations, while the transient dynamic interference method was utilized for transient calculations. The specific boundary conditions are detailed in Table 3.

During the numerical calculations, the SST (Shear Stress Transport) turbulence model was initially employed for steady-state calculations. The steady-state solution obtained from this calculation was subsequently

Table 3 Boundary conditions for numerical calculations

Fluid	Water, unsteady, incompressible
Inlet condition	Pressure
Outlet condition	Flow rate
Wall condition	No-slip wall
Computational domain interface	General Grid Interface
Convergence criterion	10^{-5}

utilized as the initial field for the transient solution using the DDES_NL method. For the transient solution, the time step was set to 1.13×10^{-4}s, and in each time step, the impeller was rotated by 1 degree. The total computation time was set to cover 10 rotation periods.

In order to facilitate the comparison and analysis between the experimental results and the numerical simulation results, the flow coefficient ϕ and the head coefficient ψ were chosen to characterize the variation law respectively (Gu et al., 2019), i.e.

$$\phi = \frac{4Q}{\pi^2 n D_2^3} \tag{18}$$

$$\psi = \frac{2gH}{\pi^2 D_2^2 n^2} \tag{19}$$

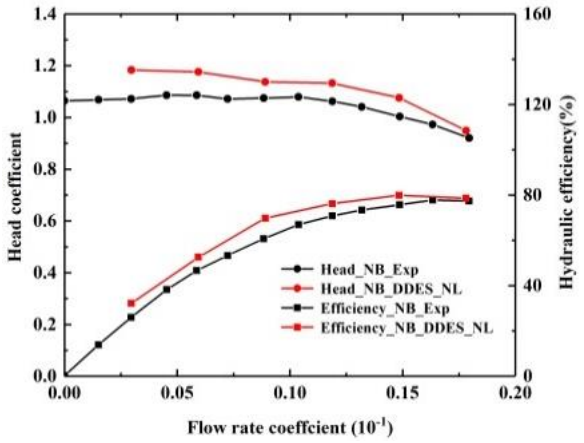

Fig. 5 Comparisons of experiments and simulations

The agreement between the numerically calculated head and efficiency and the experimental data (Zhang et al., 2021) is demonstrated in Fig 5, indicating the validity of the numerical results at various flow rates. To further validate the effectiveness of the DDES_NL model in accurately simulating the internal flow of centrifugal pumps, a comparative analysis was conducted on the experimental and numerical results of pressure pulsation inside the volute of a centrifugal pump, as illustrated in Fig 6. It should be noted that the experimental data had a higher sampling frequency compared to the numerical simulation. Additionally, the small-scale fluctuations in the flow field were approximated during the numerical calculation. As a result, there was a difference in the time resolution of the pressure pulsation signals between the two methods. Therefore, in order to ensure a fair comparison of the waveform characteristics between the experimental and numerical pressure pulsation graphs, the pressure pulsation signals were normalized. This normalization process involves mapping the used data between 0 and 1. The calculation formula used for normalization is $x_{normalization} = \frac{x - x_{\min}}{x_{\max} - x_{\min}}$. The DDES_NL model exhibited the capability to accurately capture the waveform characteristics of the pressure pulsation inside the volute of the centrifugal pump. The numerical results obtained from the model showed good agreement with the experimental data.

Figure 7 illustrates a comparison of the numerical performance characteristics among the NP, BB_1, BB_2, and BB_3. The results indicate that the NP has the greatest head and efficiency, while the head and efficiency decrease as the length of the trimming blades increases. Under rated flow conditions, the head decreases by 1.8%, 3.2%, and 5.7% for different fracture lengths, respectively, compared to normal impellers. Similarly, the efficiency decreases by 0.5%, 0.8%, and 1.0% for different fracture lengths, respectively. Similar trends were observed under other working conditions as well. This reduction in head and efficiency becomes more significant at higher flow rates, primarily due to the insufficient power provided by the trimming blades to the liquid during impeller rotation.

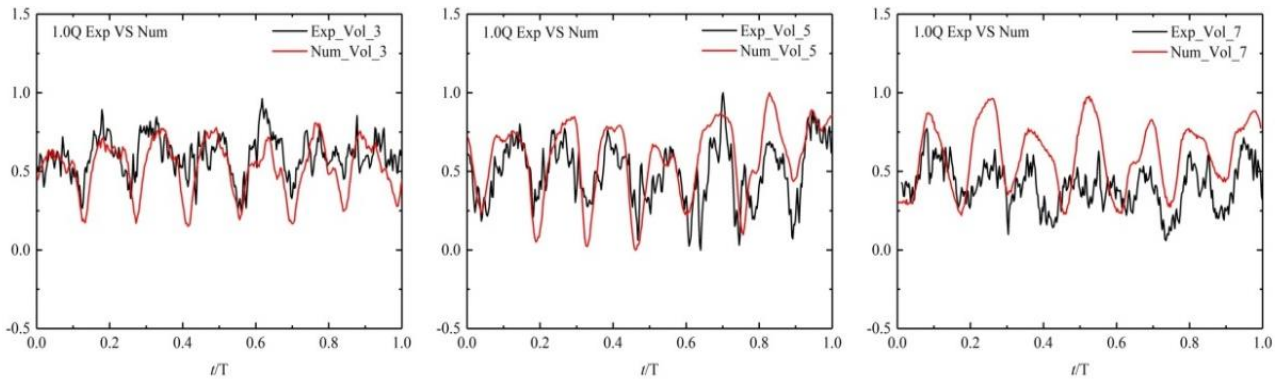

Fig. 6 Comparison of Experimental and Numerical Pressure Pulsation Waveforms inside Centrifugal Pump Volute Casing

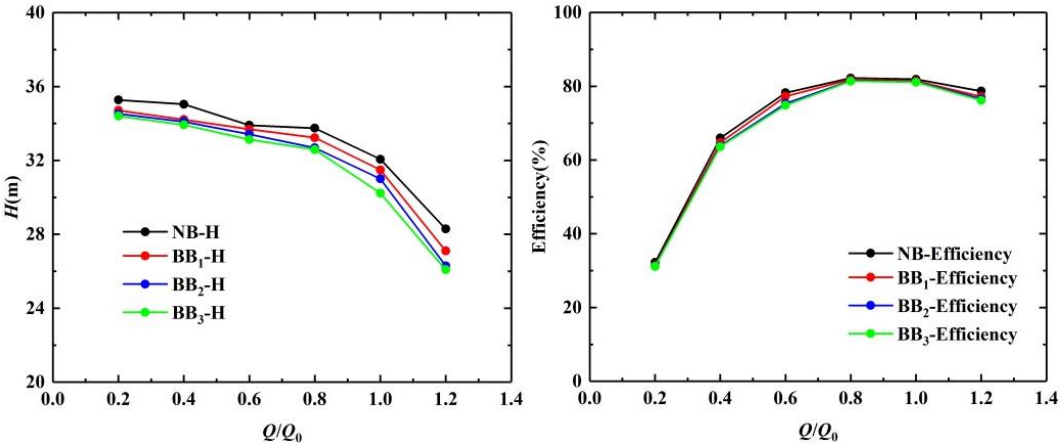

Fig. 7 Comparison of numerical performance characteristics of pump

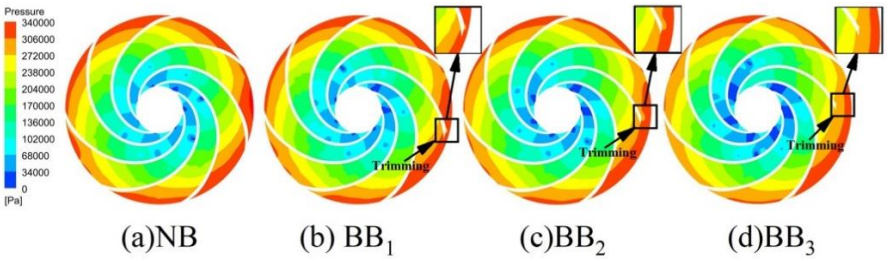

Fig. 8 Instantaneous surface pressure distribution in the impeller under 1.0Q_0

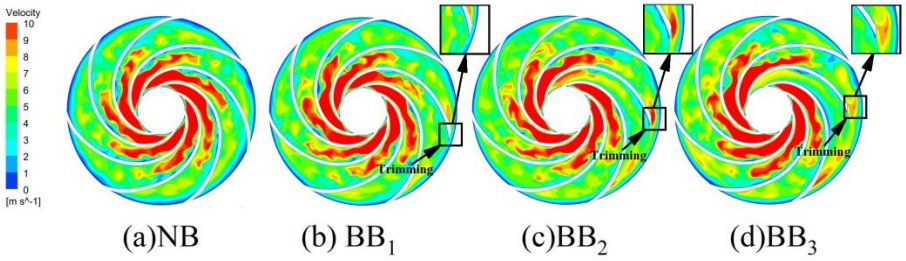

Fig. 9 Instantaneous surface velocity distribution in the impeller under 1.0Q_0

5.2. Flow Situation

Figure 8 depicts the surface pressure distribution inside the impeller at an instant. It can be observed that the NP, BB_1, BB_2, and BB_3 exhibit similar pressure distributions. Along the impeller outlet direction, the surface pressure gradually increases, with higher pressure on the pressure surface compared to the suction surface at the same radial position. Normally, the pressure distribution in each flow channel of the impeller is symmetrical. However, when a blade is trimmed, the pressure of the suction surface of the trimmed blade is higher than that on the suction surface of the normal blade at the impeller inlet. Additionally, there is a region of low pressure in other flow channels, resulting in an uneven pressure distribution inside the impeller. As the length of the trimming blade increases, the pressure at the impeller outlet gradually decreases. The presence of trimming blades significantly impacts the internal flow field pressure distribution of the impeller, primarily due to the disturbed pressure distribution in the runners adjacent to the trimming blades. This leads to higher energy losses and a reduction in the head and efficiency of the centrifugal pump, which aligns with the previous findings from comparing the centrifugal pump's external characteristic curve.

Figure 9 illustrates the instantaneous surface velocity distribution inside the impeller. The figure shows some similarities among NP, BB_1, BB_2, and BB_3. At the same radial position within the impeller, the flow velocity incrementally increases from the pressure surface to the suction surface. The NP exhibits a uniform velocity distribution in each flow channel, with the fluid velocity on the suction surface significantly higher than that on the pressure surface. The low-speed region on the blade's pressure surface and the high-speed region on the blade's suction surface are symmetrically distributed.

However, when a blade is trimmed, the velocity distribution in each flow channel becomes non-uniform. The low-speed region on the suction surface of the damaged blade expands, and the distribution becomes highly irregular. As the length of the damaged blade

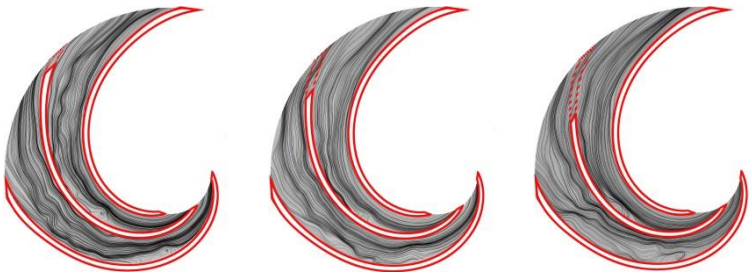

(a) BB_1 (b) BB_2 (c) BB_3

Fig. 10 zoomed-in section of streamline distribution in the impeller ($1.0Q_0$)

increases, the flow field around the trimming blades becomes more unstable. It is evident that blade damage has a significant impact on the uniformity and stability of the flow field, resulting in a loss of performance for the centrifugal pump. This loss of performance translates into a decrease in the pump's head and efficiency.

Figure 10 provides a magnified view of the streamlined distribution within the impeller. It is evident from the figure that at the exit of the trimming blade, the fluid flows from the flow channel on the pressure surface of the trimming blade to the flow channel on the suction surface of the same blade. This phenomenon obstructs the flow channel on the suction surface of the trimming blade, leading to an increase in pressure at the channel's inlet. Consequently, the flow becomes non-uniform in that region.

Figure 11 shows the transient evolution process of the middle section vortex structure in the $1.0Q_0$ operating condition of a centrifugal pump. The Q-criterion, proposed by Hunt (Hunt et al. 1988), is a widely used criterion for vortex detection. It is based on the imaginary part of the complex fluid velocity gradient tensor in the flow field to assess the strength of the vortex core. The expression for the Q-criterion in incompressible fluids is given by Equation (20):

$$Q = \frac{1}{2}\left(\left\|\Omega_{ij}\right\|_F^2 - \left\|S_{ij}\right\|_F^2\right) \tag{20}$$

Here, Ω represents the anti-symmetric part of the fluid velocity gradient tensor, and S represents the symmetric part of the fluid velocity tensor.

Inside the centrifugal pump, a strong separated vortex structure is present on the backside of the blade. As the impeller rotates, these internally separated vortices gradually develop downstream along the blade's back side, forming a wake near the blade's back side exit. This wake then enters the volute region. Over time, as the impeller continues to rotate, the wake flow structure at the blade exit is lifted and continuously sheds. The wake vortices entering the volute and the wake shedding structure at the blade exit gradually dissipate inside the volute. The diffuser tongue, located downstream of the impeller, has a significant impact on the internal flow of the centrifugal pump. When the blade passes over the diffuser tongue, the wake flow structure at the blade exit is sheared off. This shearing action results in instability and higher pressure pulsation in the internal flow of the centrifugal pump. In the case of the normal impeller, there are numerous turbulent vortex structures of various scales that are relatively evenly distributed. However, when a trimming blade is present, fewer vortex structures are observed near it. This can be attributed to the shorter length of the trimming blade, which reduces the rotational shear interaction between fluids and prevents the formation of smaller, fragmented turbulent structures. Additionally, as the distance between the blade and the break becomes shorter, the number of vortex structures near the trimming blade further decreases.

5.3. Entropy Generation Analysis

In the evaluation of energy consumption for the fault centrifugal pump using the entropy production method, two types of entropy production were considered: direct dissipation entropy production and turbulent dissipation entropy production. These types of entropy production capture the effects of instantaneous motion and velocity fluctuations, respectively. The method focused on these aspects and did not take into account wall entropy production or heat transfer entropy production.

Since water has a large specific heat capacity and the working conditions of the centrifugal pump are at normal temperature and pressure, it was assumed that there are minimal temperature changes during the process, and heat transfer effects can be neglected. Thus, the assumption of constant temperature was made, allowing the focus to be solely on the entropy production caused by fluid viscosity and turbulent fluctuations.

To differentiate between the two components, the entropy production caused by fluid viscosity was represented as "s," while the entropy production caused by turbulent fluctuations was denoted as "S" for clarity in subsequent discussions.

From the analysis of Fig 12, which shows the distribution of entropy production values, several observations can be made regarding the effects of centrifugal pump failure and the degree of damage on entropy production.

Firstly, after the centrifugal pump experiences a failure, the total entropy production significantly increases. Compared to the NB, the total entropy production of BB_1 increases by 1.16766 kg m^2 s^{-3} K^{-1}, which is a 47.59% increase. Similarly, BB_2 shows a 58.74% increase in total entropy production, with an increase of 1.44406 kg m^2 s^{-3} K^{-1}. BB_3 has the highest increase in total entropy production, with a 66.28%

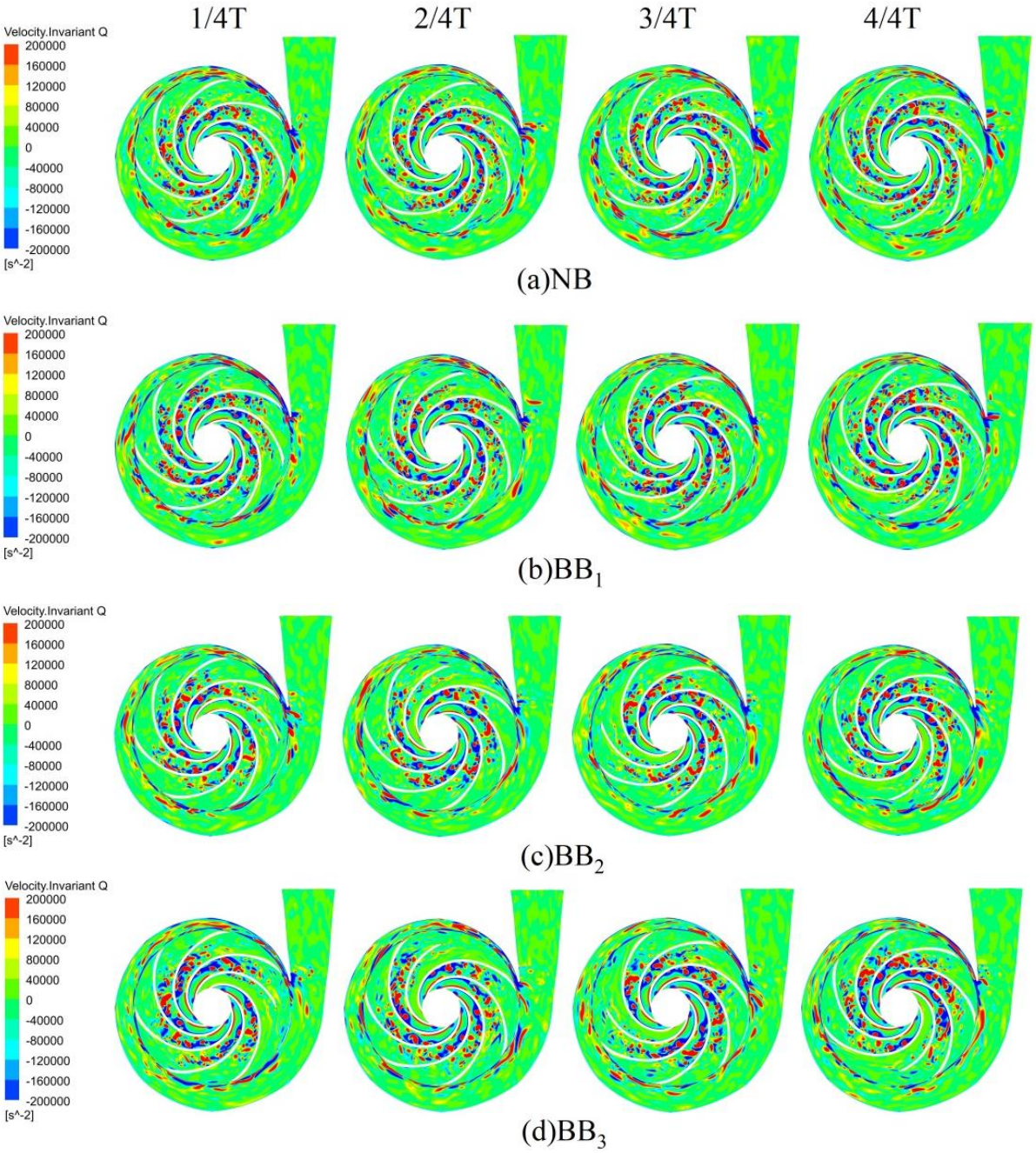

Fig. 11 Evolution process of transient vortex in the middle section of the centrifugal pump under 1.0Q_0

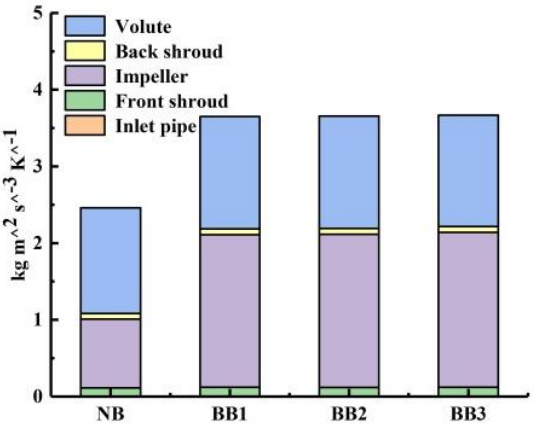

Fig. 12 Entropy production distribution of each overcurrent component under 1.0Q_0

increase and an increment of 1.6296 kg m^2 s^{-3} K^{-1}. These results indicate that as the degree of damage to the impeller increases, the irreversible losses and energy dissipation within the centrifugal pump also increase, leading to worse flow conditions inside the pump.

When examining the entropy production values of individual components, it is observed that the entropy production inside the impeller increases compared to the NB. Specifically, the entropy production value inside BB_1 impeller increases by 1.13072 kg m^2 s^{-3} K^{-1}, BB_2 impeller increases by 1.26639 kg m^2 s^{-3} K^{-1}, and BB_3 impeller increases by 1.36333 kg m^2 s^{-3} K^{-1}. Additionally, the entropy production values inside the volute also increase with damage to the impeller. The entropy production value inside BB_1 volute increases by 0.12725 kg m^2 s^{-3} K^{-1}, BB_2 volute increases by 0.18398 kg m^2 s^{-3}

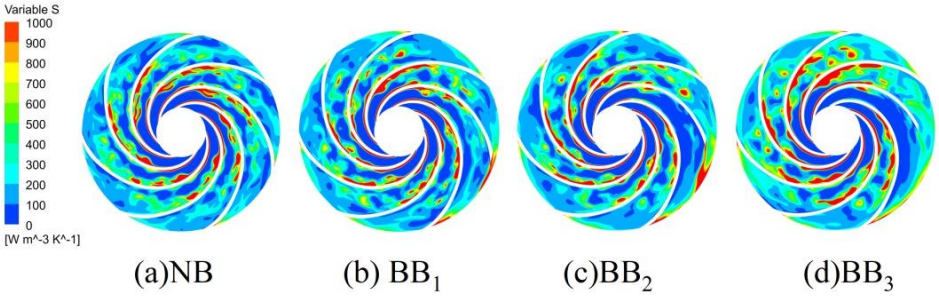

Fig. 13 Entropy production rate caused by turbulent pulsation under 1.0Q_0

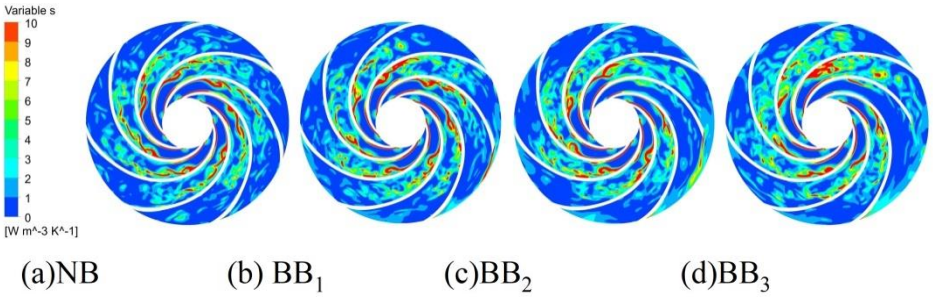

Fig. 14 Entropy production rate caused by viscous dissipation under 1.0Q_0

K^{-1}, and BB_3 volute increases by 0.27326 kg m^2 s^{-3} K^{-1}, compared to NB volute. On the other hand, the entropy production values of the front shroud and back shroud areas remain almost the same.

These findings indicate that the impeller and volute are the main locations of energy loss and entropy production in the centrifugal pump. Furthermore, it is observed that as the length of the trimming blade increases, the entropy production inside the impeller also increases, leading to more energy loss within the impeller. Therefore, it is inferred that BB_3 has more entropy production than all other impellers. It can be concluded that NB found to be better than all.

Figure 13 depicts the distribution of entropy production resulting from turbulent fluctuations inside the normal impeller and the trimming impeller under rated operating conditions. Additionally, Fig 14 displays the distribution of entropy production caused by viscous dissipation within the normal impeller and the trimming impeller at the rated operating condition.

From these figures, it can be observed that the pressure surface of the blade is the region with high entropy production caused by turbulent fluctuations and viscous dissipation. Comparing the normal impeller to the trimming impeller, it is evident that in the trimming impeller, not only the pressure surface of the blade but also the trimming region becomes a high-entropy production region. This implies that energy loss occurs in the trimming region, and as the length of the trimming region increases, the energy loss intensifies. Consequently, the head and efficiency of the centrifugal pump decrease, which aligns with the previously compared centrifugal pump characteristic curves.

The distribution of entropy production in different flow channels of the impeller varies, but overall losses

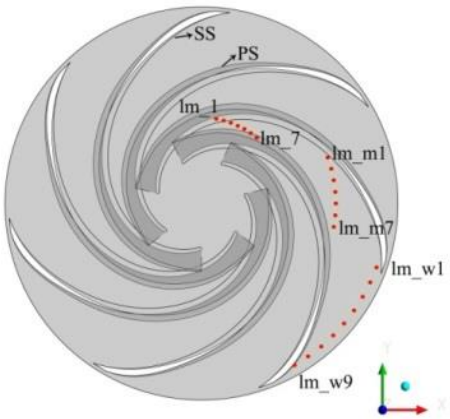

Fig. 15 Distribution of pressure fluctuation monitoring points

are substantial. The entropy production rate near the pressure surface of the blade and the suction side is significantly influenced by the adjacent wall. Notably, a considerable area with a high entropy production rate exists at the pressure surface exit of the flow channel nearest to the volute. This is mainly attributed to the generation of helical vortex structures that induce significant energy dissipation. Additionally, high-entropy production regions emerge at the head and tail of the blade due to the impact at the blade head and the jet-wake phenomenon at the blade tail.

5.4 Pressure Fluctuation and Radial Force

To investigate the pressure pulsation characteristics of marine centrifugal pumps, computational hydrodynamics was employed to conduct numerical simulations. Figure 15 illustrates the locations of monitoring points designated for measuring pressure pulsations in the impeller.

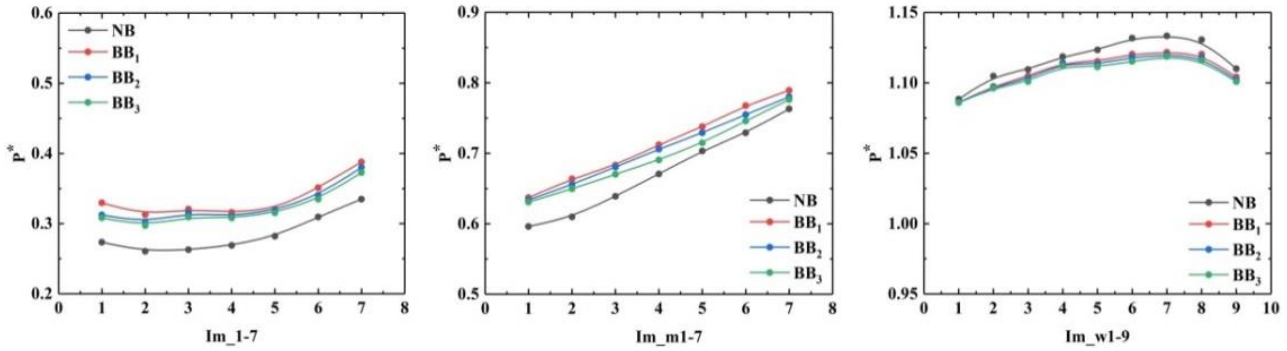

Fig. 16 Average pressure coefficient curves for each monitoring point of the centrifugal pump under 1.0Q_0

The monitoring points for pressure pulsations are arranged in a specific order. They start from the suction surface and extend to the pressure surface of the blade, located at 0.3 times the impeller radius (R_0) near the inlet of the blade, on the central plane of the impeller axis. Additionally, monitoring points are positioned at 0.5 times R_0 near the center of the impeller channel and at 0.95 times R_0 near the outlet of the blade. These monitoring points are identified as Im_i (i=1,2,...,7) for the impeller inlet points, Im_mi (i=1,2,...,7) for the impeller middle points, and Im_wi (i=1,2,...,9) for the impeller outlet points.

Calculate the mean of the instantaneous pressure at each monitoring point during the last 4 rotations of the unsteady simulation and convert it to a dimensionless value. The resulting dimensionless value is referred to as the average pressure coefficient.

$$p^* = \frac{\left(\sum_{i=1}^{N} P\right)/N}{0.5\rho U_2^{\,2}} \tag{21}$$

In the above formula, P represents the instantaneous pressure at the monitoring point in pascals, i represents the instantaneous time step, N represents the total number of time steps, ρ represents the density of water in kilograms per cubic meter, and U_2 represents the characteristic velocity in meters per second. For centrifugal pumps, the characteristic velocity is typically the circumferential speed at the impeller outlet diameter, so $U_2 = \omega D_2/2$.

Figure 16 demonstrates that the average pressure coefficient progressively increases from monitoring point Im_1-7 to Im_w1-9, indicating a rise in pressure within the impeller runner from the inlet to the outlet. The pressure coefficient on the pressure surface is greater than that on the suction surface at the same radius. The average pressure coefficient of the normal impeller exhibits the fastest increase, while that of the impeller with trimming blades shows a slower increase due to the shorter length of the trimming blades. This insufficient work leads to a decline in the performance parameters of the centrifugal pump.

The radial force acting on the impeller primarily originates from the surrounding fluid. Ideally, the radial force should be zero when the fluid entering the impeller cavity is uniformly distributed in terms of pressure and velocity, resulting in balanced forces at each location on the impeller. However, if the inflow fluid distribution is non-uniform or the flow rate deviates from rated conditions, the balance of forces will be disrupted, and the resulting radial forces will affect the steady operation of the pump. In this study, the fluid forces at each point were calculated assuming a uniform distribution of each mesh node on the impeller, using the following calculation equation:

$$C_{fri} = \frac{F_r(t_i)}{0.5\rho U_2^{\,2}\pi D_2 b_2} \tag{22}$$

Where D_2 is the diameter and b_2 is the blade width. The subscript i mean the i-th time step and $F_r(t_i)$ is the transient radial force.

Figure 17 presents the radar plot in the time domain and the frequency domain distribution of radial force coefficients for different impellers (1.0Q_0). When the centrifugal pump vanes are intact, the magnitude of the radial force on the vane surface fluctuates steadily with changes in angle, exhibiting seven crest and trough cycles, which align with the number of vanes. The radial force coefficient is smaller and more periodic under these normal conditions. This is attributed to the more uniform pressure field and velocity field inside the centrifugal pump, resulting in a more regular fluid flow and a relatively small radial force. However, when the blades are damaged, the radial force experiences distortion and the radial force coefficient become larger, surpassing the normal state. The periodicity also deteriorates. As the degree of damage increases, the radial force coefficient and the degradation in periodicity worsen.

In the normal impeller, the radial force is primarily influenced by the blade frequency (f_b), while the amplitude of the shaft frequency (f_r) is less prominent. This indicates that impeller rotation predominantly causes the radial force. However, when the impeller blades are trimmed, mass imbalance occurs in the centrifugal pump, and the radial force frequency is dominated by the characteristic shaft frequency resulting from the mass imbalance. The amplitude of the shaft frequency significantly increases, and it further intensifies as the degree of damage increases. Because when the centrifugal pump fracture failure, the fluid flow inside the centrifugal pump will become disorder, leading to increased radial force during operation and resulting in

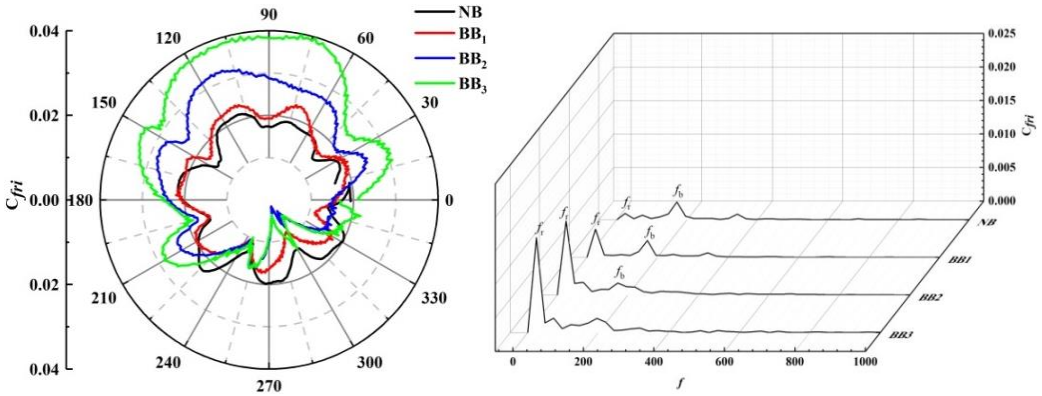

Fig. 17 Transient variation and frequency domain distribution of radial force coefficients for different impellers under 1.0Q$_0$

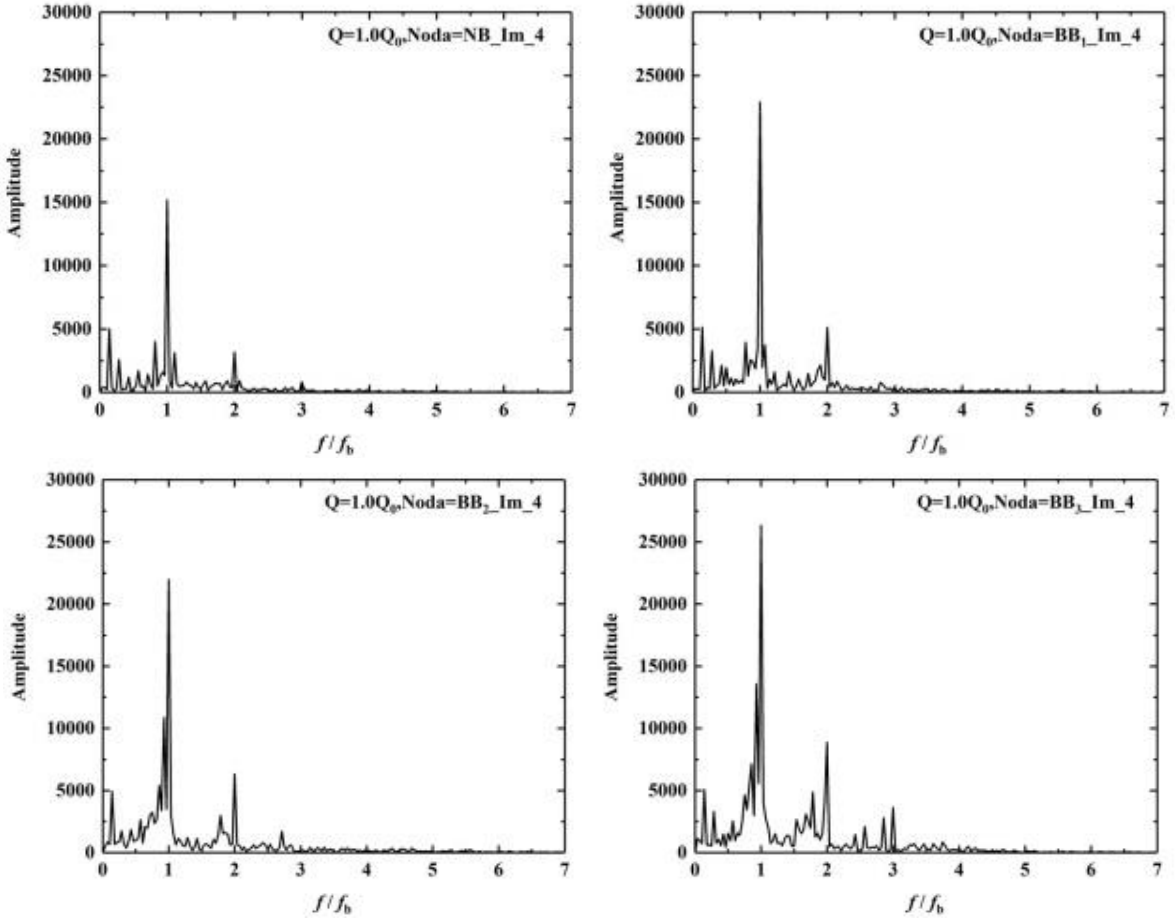

Fig. 18 Pressure fluctuation spectrum distribution at Im_4 of the impeller under 1.0Q$_0$

elevated pump vibration amplitudes, thus affecting operational stability.

The frequency domain characteristics of pressure pulsation reflect the intensity of pressure pulsation at specific frequencies. Therefore, the pressure pulsation at the rated flow rate of a centrifugal pump underwent fast Fourier transform (FFT) based on the last four rotating cycles during unsteady-state calculations to obtain the pressure pulsation characteristics in the frequency domain. To emphasize the frequency characteristics of centrifugal pump pressure pulsation, the x-axis of the spectrum graph was uniformly dimensionless with f/f_b, where f_b is the blade frequency of the centrifugal pump ($f_b = z * f_r$, where z is the number of blades and f_r is the rotational frequency).

Figure 18 displays the frequency domain diagram of pressure pulsation at monitoring point Im_4 under normal and blade trimming failure conditions. From the diagram, it is evident that the frequency components of pressure pulsation inside the normal impeller primarily consist of the rotational frequency and its harmonics. The presence of the volute disrupts the symmetry of the flow within the impeller, leading to pressure pulsation with the rotational frequency as the dominant characteristic. Blade trimming failure has a significant impact on the frequency and amplitude of pressure pulsation. When

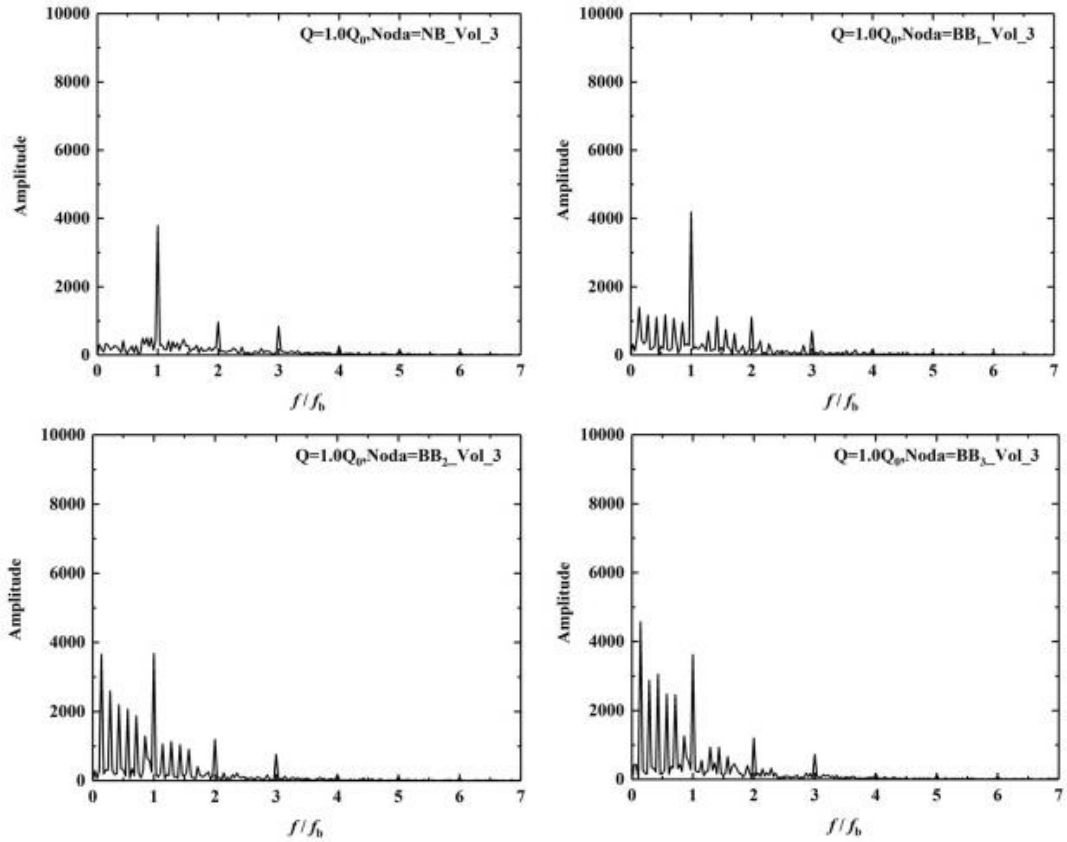

Fig. 19 Pressure fluctuation spectrum distribution at Vol_3 of the Volute under $1.0Q_0$

blade fracture failure occurs, the pressure fluctuations at the fractured blade and the adjacent blades become more pronounced, increasing the peak value of the blade frequency. The degree of fracture directly influences the magnitude of the pressure peak value in pressure pulsation.

Figure 19 depicts the frequency domain diagram of pressure pulsation at monitoring point Vol_3 under normal and blade trimming failure conditions. Inside the normal impeller vane diffuser, the pressure pulsation is primarily at the blade frequency. The trailing edge of the blade experiences local low pressure, and as the blade rotates periodically, it sweeps over fixed positions of the vane diffuser, generating pressure pulsation at the blade frequency. When blade fracture failure occurs, the rotational frequency appears in the pressure pulsation spectrum inside the vane diffuser. With an increasing degree of fracture, the presence of the rotational frequency inside the vane diffuser becomes more pronounced. Blade fracture failure can lead to abnormal pressure pulsation and abnormal vibration of the centrifugal pump.

6. CONCLUSION

This study utilized the Croe software to construct a three-dimensional structural model of a centrifugal pump for ships. Unsteady calculations were performed on the centrifugal pump using Delayed Detached Eddy Simulation (DDES) with nonlinear eddy viscosity. The flow field results were analyzed to extract information about the internal flow field, pressure pulsation, and radial force of the centrifugal pump. By employing entropy production theory, the areas of high energy loss within the centrifugal pump were identified, and the distribution characteristics of local energy loss in each component under different degrees of damage were examined. The following conclusions were drawn from the analysis:

1) As the length of damage increases, both the head and efficiency of the centrifugal pump exhibit a decreasing trend.

2) By combining numerical calculations and entropy production theory analysis of energy loss characteristics within the centrifugal pump, it was observed that irreversible loss significantly increases with the degree of damage. This indicates a deteriorating flow situation within the centrifugal pump. In comparison to a normal impeller, a damaged impeller shows high entropy production not only on the pressure surface of the blades but also at the damaged site, suggesting energy loss at the damage site. With an increase in damage length, this leads to more energy loss.

3) Blade damage causes the fluid flow within the centrifugal pump to become more unsteady, resulting in increased radial force during operation and larger vibration amplitudes. This negatively impacts the stability of the pump during operation.

4) Blade damage has a notable influence on the frequency and amplitude of pressure pulsation. When blade damage occurs, the pressure fluctuation at the damaged and adjacent blades becomes more severe, leading to an increase in the peak value of the blade

frequency. As the degree of damage increases, the pressure fluctuation and peak value of pressure pulsation also increase. These abnormal pressure pulsations can induce abnormal vibrations in the centrifugal pump. Therefore, monitoring pressure pulsation can serve as an early warning and diagnostic method for detecting blade damage.

ACKNOWLEDGMENTS

This was financially supported by the National Natural Science Foundation of China (Grant No. 12172208).

CONFLICT OF INTEREST

The authors declare that they have no competing interests.

AUTHORS CONTRIBUTION

L.J. Zhai: performed the data analyses and Writing the original draft; H.X. Chen: Supervision, review and editing; Qi Gu: review and editing; Z. Ma: Supervision, review and editing.

REFERENCES

Aenis, M., Knopf, E., & Nordmann, R. (2002). Active magnetic bearings for the identification and fault diagnosis in turbomachinery. *Mechatronics*, 12(8), 1011-1021. https://doi.org/10.1016/S0957-4158(02)00009-0.

Araste, Z., Sadighi, A., & Moghaddam, M. J. (2020). *Support vector machine-based fault diagnosis of a centrifugal pump using electrical signature analysis*. 2020 6th Iranian Conference on Signal Processing and Intelligent Systems (ICSPIS).

Behzadmehr, A., & Mercadier, Y. (2009). Numerical study of flow parameters and entropy generation on a centrifugal fan. *International Journal of Exergy*, 6(1), 80-92. https://doi.org/10.1504/ijex.2009.023346.

Brizuela, E. A. (1993). *Numerical modeling of entropy generation and transport in the Blade-Tip gap layer of a radial impeller*. ASME 1993 International Gas Turbine and Aeroengine Congress and Exposition. American Society of Mechanical Engineers, V001T03A026-V001T03A026. https://doi.org/10.1115/93-GT-085.

Cao, S., Hu, Z., Luo, X., & Wang, H. (2020). Research on fault diagnosis technology of centrifugal pump blade crack based on PCA and GMM. *Measurement*, 173(4), 108558. https://doi.org/10.1016/j.measurement.2020.108558.

Champagne, F., Harris, V., & Corrsin, S. (1970). Experiments on nearly homogeneous turbulent shear flow, *Journal of Fluid Mechanics*, 41(1), 81-139. https://doi.org/10.1017/S0022112070000538

Chen, X. R. (2020). *Research on the operating characteristics of marine centrifugal pumps*. Jiangsu University. https://doi.org/10.27170/d.cnki.gjsuu.2020.000160

Chen, Z. D., Yang, S. D., Li, X. J., Li, Y. P., & Li, L. M. (2023). Investigation on leakage vortex cavitation and corresponding enstrophy characteristics in a liquid nitrogen inducer. *Cryogenics*, 129, 103606. https://doi.org/10.1016/j.cryogenics.2022.103606.

Feng, L. G. (2021). Research on the detection of GNSS phase center deviation using relative positioning method. *Shaanxi Transportation Science and Education Research*, 5-9. http://qikan.cqvip.com/Qikan/Article/Detail?id=7105239748

Gong, R. Z., Wang, H. J., & Chen, L. X. (2013). Application of entropy production theory to hydro-turbine hydraulic analysis. *Science China Technological Sciences*, 56(7), 1636-1643. https://doi.org/10.1007/s11431-013-5229-y

Gu, Y. D., Pei, J., Yuan, S. Q., Wang, W. J., Zhang, F., Wang, P., Appiah, D., & Liu, Y. (2019). Clocking effect of vaned diffuser on hydraulic performance of high-power pump by using the numerical flow loss visualization method. *Energy*, 170(MAR.1), 986-997. https://doi.org/10.1016/j.energy.2018.12.204

Hu, Z. J. (2019). *Research on fault diagnosis technology for cracks in single stage and single suction centrifugal pump blades*. Wuhan: Huazhong University of Science and Technology. https://doi.org/10.27157/d.cnki.ghzku.2019.004578

Hunt, J. C. R., Wray, A. A., & Mon, P. (1988). Eddies, streams, and convergence zones in turbulent flows. *Center. for turbulence research*. https://web.stanford.edu/group/ctr/Summer/2013061 11537.pdf.

Jamimoghaddam, M., Sadighi, A., & Araste, Z. (2020). *ESA-Based anomaly detection of a centrifugal pump using Self-Organizing map.* 2020 6th Iranian Conference on Signal Processing and Intelligent Systems (ICSPIS).

Kock, F., & Herwig, H. (2004). Local entropy production in turbulent shear flows: A high-Reynolds number model with wall functions. *International Journal of Heat and Mass Transfer*, 47(10), 2205- 2215. https://doi.org/10.1016/j.ijheatmasstransfer.2003.11.025

Kock, F., & Herwig, H. (2005). Entropy production calculation for turbulent shear flows and their implementation in CFD codes. *International Journal of Heat and Fluid Flow*, 26(4), 672-680. https://doi.org/10.1016/j.ijheatfluidflow.2005.03.005

Lan, J. (2020), *Study on Fault Characteristics of Ship Centrifugal Pump Based on CFD*. Dalian University of Technology, Dalian, China. https://doi.org/10.26991/d.cnki.gdllu.2020.002581

Lee, M. J., Kim, J., & Moin, P. (1990). Structure of

turbulence at high shear rate, *Journal of Fluid Mechanics*, 216, 561-583. https://doi.org/10.1017/S0022112090000532

Li, D. Y., Wang, H. J., Qin, Y. L., Han, L., Wei, X., & Qin, D. (2021). Entropy production analysis of hysteresis characteristic of a pump-turbine model. *Energy Conversion and Management*, 149, 175-191. https://doi.org/10.1016/j.enconman.2017.07.024

Li, X. J., Ouyang, T., Lin, Y. P., & Zhu, Z. C. (2023). Interstage difference and deterministic decomposition of internal unsteady flow in a five-stage centrifugal pump as turbine. *Physics of Fluids*, 35(4), 045136. https://doi.org/10.1063/5.0150300

Li, Y. J., Liu, Q., & Li, W. (2023). Research and application of intelligent diagnosis method for impeller faults based on digital twin flow field cloud map of centrifugal pumps. *Journal of Beijing University of Aeronautics and Astronautics*, 1-11. https://doi.org/10.13700/j.bh.1001-5965.2022.0997

Li, Y., Wang, X., & Si, S. (2018). *Centrifugal pumps fault diagnosis using multivariate multiscale symbolic dynamic entropy and logistic regression.* Prognostics and System Health Management Conference. https://sci-hub.st/10.1109/phm-chongqing.2018.00078

Liu, C., Chen, H. X., & Ma, Z. (2022). Influence of non-uniform inflow on unsteady internal flow characteristics of waterjet pump. *Modern Physics Letters B*, 36(05). https://doi.org/10.1142/S021798492150576X

Muralidharan, V., Sugumaran, V., & Sakthivel, N. R. (2011). Wavelet decomposition and support vector machine for fault diagnosis of monoblock centrifugal pump. *International Journal of Data Analysis Techniques & Strategies*. 3(2), 159-177. https://doi.org/10.1504/IJDATS.2011.039849

Ohiemi, I. E., Yang, S. S., Singh, P., Li, Y. J., & Osman, F. (2023). Evaluation of energy loss in a low-head axial flow turbine under different blade numbers using entropy production method. *Energy*, 274, 127262. https://doi.org/10.1016/j.energy.2023.127262

Rogers, M. M., & Moin, P. (1987). The structure of the vorticity field in homogeneous turbulent flows. *Journal of Fluid Mechanics*, 176, 33-66. https://doi.org/10.1017/S0022112087000569

Seo, D. H., & Lee, D. J. (2019). Numerical investigation of highly unsteady accelerated/decelerated flows for blunt bodies experiencing impulsive motion. *Physics of Fluids*, 31(5). https://doi.org/10.1063/1.5089674

Spalart, P. R., Jou, W. H., & Strelets, M. (1997). *Comments on the feasibility of LES for wings and on a hybrid RANS/LES approach.* Proceedings of 1st AFOSR International Conference on DNS/LES, Advances in DNS /LES. Columbus: Greyden Press, 137-147. https://www.researchgate.net/profile/Michael-Strelets/publication/236888805_Comments_on_the_Feasibility_of_LES_for_Wings_and_on_a_Hybrid_RANSLES_Approach/links/0c9605232f307402e8000000/Comments-on-the-Feasibility-of-LES-for-Wings-and-on-a-Hybrid-RANS-LES-Approach.pdf.

Tan, M., Lu, Y., Wu, X., Liu, H., & Tian, X. (2020). Investigation on performance of a centrifugal pump with multi-malfunction. *Journal of Low Frequency Noise Vibration and Active Control*, 40(2):146134842094234. https://doi.org/10.1177/1461348420942349.

Tavoularis, S., & Corrsin, S. (1981). Experiments in nearly homogenous turbulent shear flow with a uniform mean temperature gradient. Part 1, *Journal of Fluid Mechanics*, 104,311-347. https://doi.org/10.1017/S0022112081002930.

Wallace, J. D., & Davies, M. (1997*). Entropy generation measurement in a laminar turbine blade boundary-layer*. ASME 1997 International Gas Turbine and Aeroengine Congress and Exhibition， American Society of Mechanical Engineers.

Wang, S. L., Zhang, L., Ye, X. M., & Wu, Z. (2011). Performance optimization of centrifugal fan based on entropy generation theory. *Proceedings of the CSEE*, 31(11), 86-91. https://doi.org/10.1631/jzus.A1000257.

Wang, S., Yang, S., Shao, C. L., & Zhou, J. F. (2023). Impact of transient gas injection on flow-induced noise in centrifugal pumps. *Journal of Applied Fluid Mechanics*, 16(3), 477-489. https://doi.org/10.47176/JAFM.16.03.1284.

Wang, X. L., Wang, Y., Liu, H. L., Xiao, Y. D., Jiang, L. L., & Li, M. (2023). A numerical investigation on energy characteristics of centrifugal pump for cavitation flow using entropy production theory. International *Journal of Heat and Mass Transfer*, 201, 123591. https://doi.org/10.1016/j.ijheatmasstransfer.2022.123591.

Wang, X., Yan, Y., Wang, W. Q., & Hu, Z. P. (2023). Evaluating energy loss with the entropy production theory: A case study of a micro horizontal axis river ducted turbine, *Energy Conversion and Management*, 276, 116553. https://doi.org/10.1016/j.enconman.2022.116553.

Wang, Y. (2019). *Improvement and application of rans/les turbulence model based on turbulent flow field with curvature and rotation effect*. Jiangsu University, Zhenjiang, China. https://kns.cnki.net/kcms2/article/abstract?v=3uoqIhG8C475KOm_zrgu4lQARvep2SAkOsSuGHvNoCRcTRpJSuXuqSPO-8wiUoEWkx3pr3no99l1Zn_G6Vrho3Nl5Asm177j&uniplatform=NZKPT.

Wei, Q., Chen, H. X., & Ma, Z. (2015). *Numerical simulation of flow around airfoil with Non-Linear RANS model, Proc.* ASME/JSME/KSME 2015 Joint Fluids Engineering Conference, American Society of Mechanical Engineers, V01AT02A014-

V001AT002A014.

Wei, Q., Chen, H. X., Ma, Z. (2016). An hybrid RANS/LES model for simulation of complex turbulent flow. *Journal of Hydrodynamics*, 28(5), 811-820. https://doi.org/10.1016/S1001-6058(16)60684-4.

Wu, X. F., Sun, X. L., Tan, M. G., & Liu, H. L. (2021). Research on operating characteristics of a centrifugal pump with broken impeller. *Advances in Mechanical Engineering*, 13, 9. https://doi.org/10.1177/16878140211049951.

Yang, H. (2019). *Optimization of impeller parameters and study of typical fault diagnosis for centrifugal pumps*. Yanshan University, Hebei, China. https://doi.org/10.27440/d.cnki.gysdu.2019.000388.

Zabihihesari, A., Shirazi, F. A., Riasi, A., Mahjoob, M. , & Asnaashari, E. (2020). Simulation-based vibration sensor placement for centrifugal pump impeller fault detection. *Journal of Computational Applied Mechanics*, 51(1), 72-80. https://doi.org/10.22059/jcamech.2020.298391.485.

Zhai, L. J., Chen, H. X., & Ma, Z. (2022). A delayed detached eddy simulation model for the simulation of complex turbulent flow. *Journal of Applied Fluid Mechanics*, 15(4), 1111-1124. https://doi.org/10.47176/JAFM.15.04.1061.

Zhang, J. (2017). *Research on the operating characteristics of marine centrifugal pumps under typical fault conditions*. Jiangsu University. https://kns.cnki.net/kcms2/article/abstract?v=3uoqIhG8C475KOm_zrgu4lQARvep2SAk-6BvX81hrs37AaEFpExs0JXM5APDPeb0NIKM4j3qVgddU1FGMDdOS_4w_ecw3LBr&uniplatform=NZKPT.

Zhang, S. W., Chen, H. X., & Ma, Z. (2021). A modified filter-based model for simulation of unsteady cavitating flows around a NACA66 hydrofoil, *Modern Physics Letters B*, 35(1), 2150032. https://doi.org/10.1142/S0217984921500329.

Zhang, S. W., Chen, H. X., Ma, Z., Wang, D. F., Ding, K. J. (2022a). Unsteady flow and pressure pulsation characteristics in centrifugal pump based on dynamic mode decomposition method. *Physics of Fluids*, 34, 112014-1-112014-21. https://doi.org/10.1063/5.0097223.

Zhang, S. W., Tian, R. Q., Ding, K, J., Chen, H. X., & Ma, Z. (2022b). Numerical and experimental study in pressure pulsation and vibration of a two-stage centrifugal pump under cavitating condition. *Modern Physics Letters B*, 36(1), 2150501. https://doi.org/10.1142/S0217984921505011.

Zhang, X., Wang, Y., & Xu, X. M. (2011). Internal energy conversion characteristics of low specific speed centrifugal pump impellers. *Transactions of the Chinese Society for Agricultural Machinery*, 42(7), 75-81. https://doi.org/10.3969/j.issn.1000-12985.

Zhang, Z., Chen, H. X., Ma, Z., He, J., & Liu, C. (2019a). Research on improving the dynamic performance of centrifugal pumps with twisted gap drainage blades. *Journal of Fluids Engineering*, 141(9), 1-15. https://doi.org/10.1115/1.4042885.

Zhang, Z., Chen, H. X., Ma, Z., Wei, Q., He, J., Liu, H., & Liu, C. (2019b). Application of the hybrid RANS/LES method on the hydraulic dynamic performance of centrifugal pumps. *Journal of Hydrodynamics*, 31(3), 637-640. https://doi.org/10.1007/s42241-018-0150-2.

Zhang, Z., Chen, H., Yin, J., Ma, Z., Gu, Q., Lu, J., & Liu, H. (2021). Unsteady flow characteristics in centrifugal pump based on proper orthogonal decomposition method. *Physics of Fluids*, 33(7), 075122. https://doi.org/10.1063/5.0058553.

Zhou, L., Hang, J. W., & Bai, L. (2022). Application of entropy production theory for energy losses and other investigation in pumps and turbines: A review. *Applied Energy*, 318. https://doi.org/10.1016/J.APENERGY.2022.119211.

Zhu, J. (2016). *Analysis of performance degradation mechanism and diagnostic method for multi-stage centrifugal pump faults*. Beijing University of Chemical Technology, Beijing, China. https://kns.cnki.net/kcms2/article/abstract?v=3uoqIhG8C475KOm_zrgu4lQARvep2SAkkyu7xrzFWukWIylgpWWcEi6oSS-yoCOQ0JnsK3OJFB9bihmOhmnCROaj4pMD8AE0&uniplatform=NZKPT.